Cell Reports
Physical Science

CellPress
OPEN ACCESS

Article

Atomic structures of naphthalene dipeptide micelles unravel mechanisms of assembly and gelation

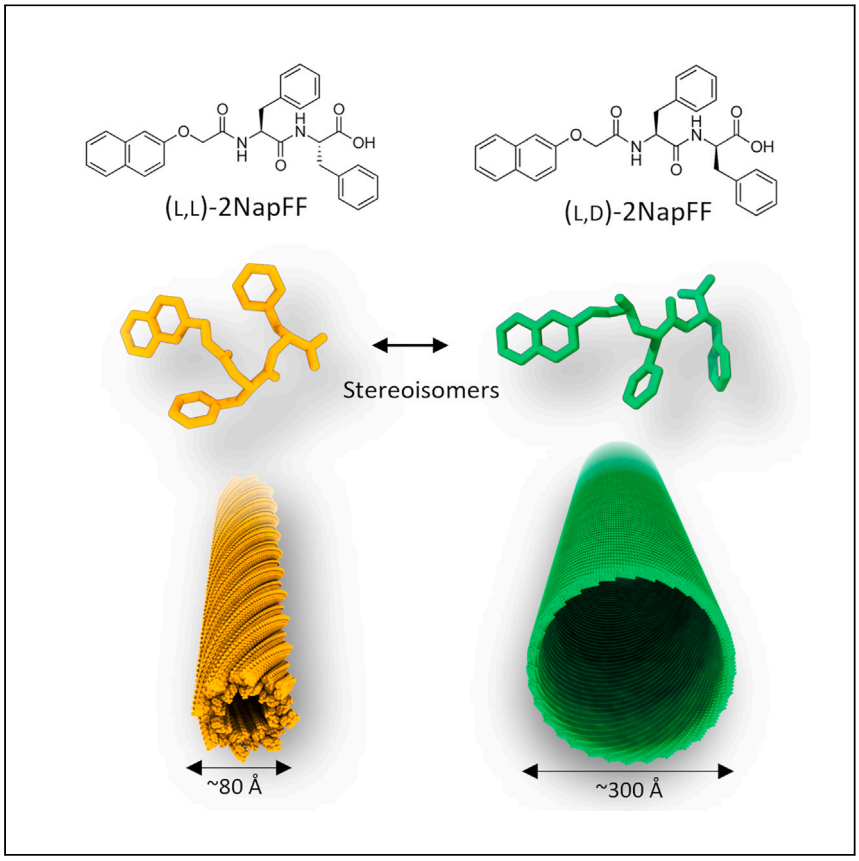

Sonani et al. study the assembly of a naphthalene dipeptide (2NapFF) in homochiral and heterochiral tubes, which form supramolecular gels. Using cryo-EM, the structures of LL- and LD-tubes are related to the configuration of the dipeptide, revealing how aromatic rings' π-π stacking and carbonyl group repulsion shape these structures.

Ravi R. Sonani, Simona Bianco, Bart Dietrich, James Doutch, Emily R. Draper, Dave J. Adams, Edward H. Egelman

dave.adams@glasgow.ac.uk (D.J.A.)
egelman@virginia.edu (E.H.E.)

Highlights

Atomic structures of 2NapFF micelles are solved by cryo-EM

Aromatic rings' π-π stacking and repulsion between carbonyls shape 2NapFF micelles

Structural analysis of 2NapFF micelles reveals the mechanism underlying gelation

Sonani et al., Cell Reports Physical Science 5, 101812
February 21, 2024
https://doi.org/10.1016/j.xcrp.2024.101812

Cell Reports
Physical Science

CellPress
OPEN ACCESS

Article

Atomic structures of naphthalene dipeptide micelles unravel mechanisms of assembly and gelation

Ravi R. Sonani,[1] Simona Bianco,[2] Bart Dietrich,[2] James Doutch,[3] Emily R. Draper,[2] Dave J. Adams,[2,*] and Edward H. Egelman[1,4,*]

SUMMARY

Peptide-based biopolymers have gained increasing attention due to their versatile applications. A naphthalene dipeptide (2NapFF) can form chirality-dependent tubular micelles, leading to supramolecular gels. The precise molecular arrangement within these micelles and the mechanism governing gelation have remained enigmatic. We determined, at near-atomic resolution, cryoelectron microscopy structures of the 2NapFF micelles LL-tube and LD-tube, generated by the stereoisomers (L,L)-2NapFF and (L,D)-2NapFF, respectively. The structures reveal that the fundamental packing of dipeptides is driven by the systematic π-π stacking of aromatic rings and that same-charge repulsion between the carbonyl groups is responsible for the stiffness of both tubes. The structural analysis elucidates how a single residue's altered chirality gives rise to markedly distinct tubular structures and sheds light on the mechanisms underlying the pH-dependent gelation of LL- and LD-tubes. The understanding of dipeptide packing and gelation mechanisms provides insights for the rational design of 2NapFF derivatives, enabling the modulation of micellar dimensions.

INTRODUCTION

Short peptides are now well-established building blocks for a range of useful supramolecular materials.[1–7] In addition, there is much to be learned from the self-assembly of synthetic oligopeptides with regard to biological processes, including the misfolding of proteins that lead to diseases such as amyloid and Huntington's.[8,9] There is huge diversity in the short peptides that have been examined, and the resulting range of self-assembled structures that can be formed is also large.[5,10–12] Self-assembled aggregates that have been reported include tapes, tubes, fibers, spherical structures, helices, two-dimensional (2D) films, and toroids.[13] These aggregates often have a hierarchical assembly and can further form larger structures and useful materials. For example, it is not uncommon for gels to be formed from the aggregation of 1D structures such as fibers or nanotubes.[14]

A key question, especially from the perspectives of rational design and of extrapolating understanding to biological processes, is how the peptides pack within the self-assembled structures. Different properties result from the same short peptide self-assembled in different ways,[15] and it is clearly important to understand why this is the case. Further, if one wants to carry out selective reactions on a self-assembled aggregate, it is necessary to know whether specific functional groups are accessible.

[1]Department of Biochemistry and Molecular Genetics, University of Virginia, Charlottesville, VA 22903, USA

[2]School of Chemistry, University of Glasgow, G12 8QQ Glasgow, UK

[3]ISIS Pulsed Neutron and Muon Source, Harwell Science and Innovation Campus, OX11 0QX Didcot, UK

[4]Lead contact

*Correspondence: dave.adams@glasgow.ac.uk (D.J.A.), egelman@virginia.edu (E.H.E.)

https://doi.org/10.1016/j.xcrp.2024.101812

It is relatively easy to visualize the larger aggregates that are formed using techniques such as negative-stain transmission electron microscopy or atomic force microscopy and to use small-angle scattering to determine some structural parameters in the formation of fibers or helical tapes.[16] However, such techniques do not necessarily provide insight into the atomic structures. Infrared spectroscopy and circular dichroism can potentially provide insight into the arrangement of the peptides, and it can be possible to interpret spectroscopic data as showing that the peptides form β-sheets or α-helices.[16] Caution is required here, especially for short, functionalized peptides, as it is not always clear that the data from such well-studied systems as poly(lysine) can be extrapolated to, for example, dipeptides. However, it is still common to see reports using such information to provide a detailed cartoon as to molecular packing with little concrete evidence. There is a belief that solving a crystal structure or collecting powder X-ray diffraction data on a sample (usually dried) can be informative.[17–20] However, it is clear, at least in some cases for the dipeptides discussed in this paper, that such approaches are not always useful. For example, for a dipeptide-based gel, the structure of a crystal grown directly from the gel phase does not agree with the fiber diffraction data from the gel phase, showing that the molecular packing must be different.[21] Similarly, drying often leads to changes in morphology,[22] meaning that extrapolation from data on dried samples to solvated supramolecular structures should be treated with caution. In structural biology, it has been well established for more than 80 years that the structure of a protein or protein crystal is only maintained when it is fully hydrated,[23] and it is inconceivable that most peptides would behave differently.

Contrast-matching small-angle neutron scattering (SANS) approaches with selectively deuterated analogs of a functionalized dipeptide have been used to understand the molecular packing in a micellar and gel state.[24] This approach allowed molecular-level information to be accessed, but this method requires extensive synthesis, access to competitive beamtime at large-scale facilities, long data collection times, and models fit to the data that may not be unique. Further, one must assume that such selective deuteration does not change the molecular self-assembly. A more accessible technique is therefore required to determine structures of these assemblies at near-atomic resolution. One method that is providing high-resolution structures for many proteins is cryoelectron microscopy (cryo-EM), which has emerged over the past 10 years as the dominant technique in structural biology of macromolecular complexes.[25–27] Although the applications of cryo-EM to peptides have been rather limited, they are rapidly growing.[28,29]

It has been demonstrated that the naphthalene-conjugated dipeptide possesses better biocompatibility.[30] Extensive investigations have been conducted on various derivatives within this novel class of gelators, as reviewed in Hamley.[31] Specifically, functionalized analogs of diphenylalanine are widely used and have been shown to be highly effective gelators.[32–36] The self-assembly of a naphthalene dipeptide (2NapFF; Figure 1) forming gels with different rheological properties has been previously studied widely by the Adams group.[24,37] 2NapFF, like a surfactant, undergoes concentration-dependent structural transformation from free molecules to worm-like micelles at alkaline pH, followed by the association of these worm-like micelles into a gel at neutral to acidic pH.[24,38] The molecular packing of worm-like micelles has only been predicted by molecular dynamics or modeled into low-resolution data from SANS and small-angle X-ray scattering (SAXS).[24,38] Thus, the actual molecular packing of these micelles remains undetermined. Here,

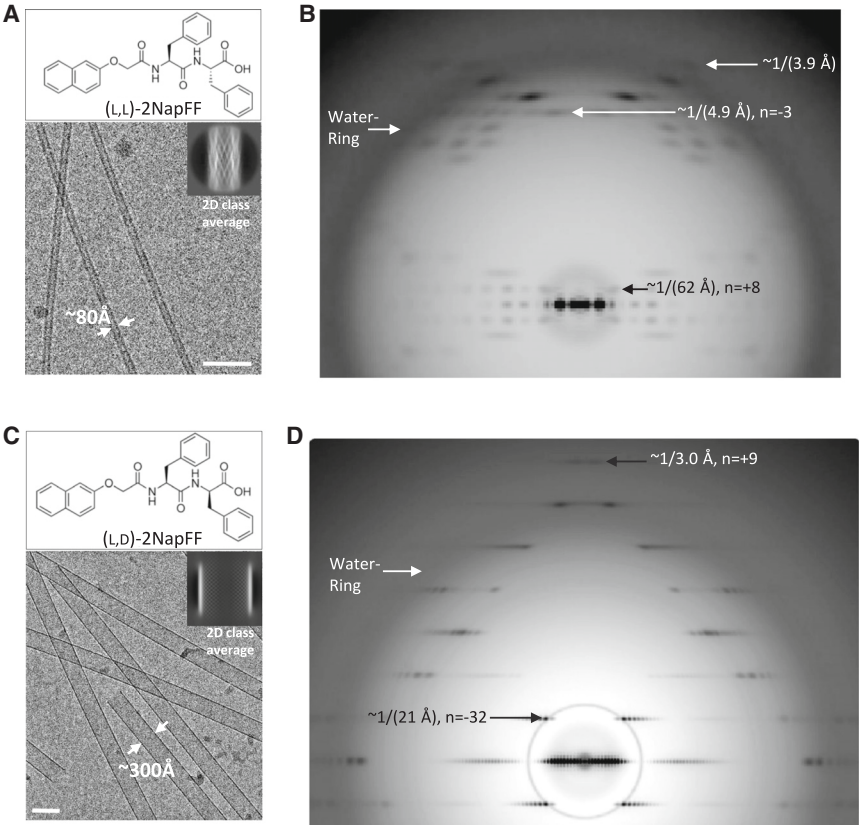

Figure 1. Morphology of the self-assembled LL- and LD-tubes

(A) Chemical structure of (L,L)-2NapFF dipeptide (top) and cryo-EM with 2D class average of LL-tube (bottom).

(B) Averaged power spectrum of LL-tube segments. Three layer lines with their associated Bessel orders are labeled. The diffuse water ring, at ~ 1/(3.7 Å), arises from the average separation of water molecules being ~3.7 Å.

(C) Chemical structure of (L,D)-2NapFF dipeptide (top) and cryo-EM with 2D class average of LD-tube (bottom).

(D) Averaged power spectrum of LD-tube segments, with two layer lines and the water ring labeled. The self-assembly of the here-shown LL- and LD-tubes was induced by continuous stirring of 1% peptide solution at pH 11 and room temperature. Scale bar: ~50 nm.

we directly determine the molecular packing of these dipeptides by cryo-EM. Our results reveal how the small peptide assembles into giant and ordered micelles and, further, how the chirality of the dipeptide dramatically changes the packing, shape, and size of the resultant micelles.

RESULTS

Self-assembly of (L,L)-2NapFF and (L,D)-2NapFF micelles

The (L,L)-2NapFF dipeptide is a very simple chemical structure—a naphthalene attached to the N terminus of diphenylalanine (Figure 1A). The (L,D)-2NapFF is a stereoisomer of the (L,L)-2NapFF, as its second Phe is a *D* isoform (Figure 1C). The self-assembly of dipeptides (L,L)-2NapFF and (L,D)-2NapFF into micelles is induced by continuous stirring of 1% peptide solutions at pH 11 and room temperature. After overnight stirring, they polymerize into long tubular micelles of ~80 and ~300 Å diameter, respectively, which we name LL- and LD-tubes (Figures 1A and 1C).

Cryo-EM structure of (L,L)-2NapFF micelle

Movies are acquired rather than single images, taking advantage of the extremely fast frame rates of the direct electron detector cameras. These movies allow one to correct for beam-induced motion during the imaging. One can then determine the defocus that was present to generate the phase contrast for each image and use this to correct for the phase reversals that occur in the contrast transfer function (CTF). Automated methods are then used to cut segments from the tubes. A 2D class average from 427,056 segments (Figure 1A) shows high-resolution features, and these periodic high-resolution features are also apparent in the averaged power spectrum of LL-tube segments (Figure 1B), with layer lines (ll) arising from the helical symmetry extending out to 3.9 Å resolution. This suggests that, unlike amorphous lipid micelles, the LL-tube has highly ordered packing. The helical symmetry that we determined for this tube was an axial rise of 0.59 Å and a helical rotation of −134.57° relating each asymmetric unit (ASU). We have used 3D reconstruction from the 2D segments, and the map shows clear density for the phenylalanine side chains, the naphthalene aromatic rings, and the peptide backbone, allowing for an atomic model to be built with high confidence (Figure 2A). It is of note that the map-to-map Fourier shell correlation (FSC), which has been called a "gold standard" in estimating resolution in structural biology,[39] overestimates the resolution of the map to be 2.7 Å (Figure S1). In contrast, the map-to-model FSC[40] yields a value of 3.3 Å, which is much more consistent with the visual features of the map. The LL-tube is an eight-start helix consisting of eight protofilaments, where each protofilament is formed by three strands, two outer and one inner (Figures 2A and 2B). The helical ASU of the LL-tube is a trimer of dipeptides, with one forming the inner wall and two forming the outer wall. There is an intrinsic enantiomorphic ambiguity in 3D maps generated by cryo-EM due to the fact that projection images have been collected.[28] In protein structures, a resolution better than ∼4.5 Å will show a hand for α-helices that will allow for the determination of which of the two enantiomorphic volumes is the correct one. For proteins or peptides that contain no α-helices, the hydrogen-bonding pattern in β-sheets can be used when the resolution is ∼2.5 Å or better.[41] For the LL-tubes, it was difficult to determine the correct hand of the map due to the absence of a regular secondary structure. For the determination of the hand, we built LL-tube atomic models (containing ∼75 copies of the dipeptide) into both the right- and left-handed maps and ran the *Real-space refinement* and *Molprobity* validations in Phenix. The C_β-outliers in the left-handed model (∼33.3%) are double those of the right-handed (∼16.7%) map, indicating that the right-handed map is most likely the correct one. Moreover, the H-bond distance, ∼3.4 Å (see below), in the right-handed model is consistent among the three strands, suggesting that the strands are indeed right-handed.

There are three conformations of the dipeptide present, as each dipeptide in the ASU adopts a different conformation. The conformations of the two outer dipeptides are similar, while the inner dipeptide has a completely different conformation (Figure 2B). Looking from the top, the inner dipeptide orients all aromatic rings (naphthalene and two Phe rings) on the same side of the peptide back bone, whereas in both outer dipeptides, the second Phe ring flips to the opposite side of the peptide backbone (Figure 2C). The stacking of dipeptides within each strand is mainly mediated by the π-π stacking of all three aromatic rings with an average (ring center-to-center) stacking distance of 5.0 ± 0.1 Å (Figure 2D). The packing involves a weak H-bond between a carbonyl oxygen and a naphthalene-connecting nitrogen in the inner strand and between a carbonyl oxygen and an amide nitrogen in both outer strands (Figure 2D). With this packing, dipeptides bury all their aromatic rings in the lumen between the outer and inner walls of the LL-tube, exposing the carbonyl

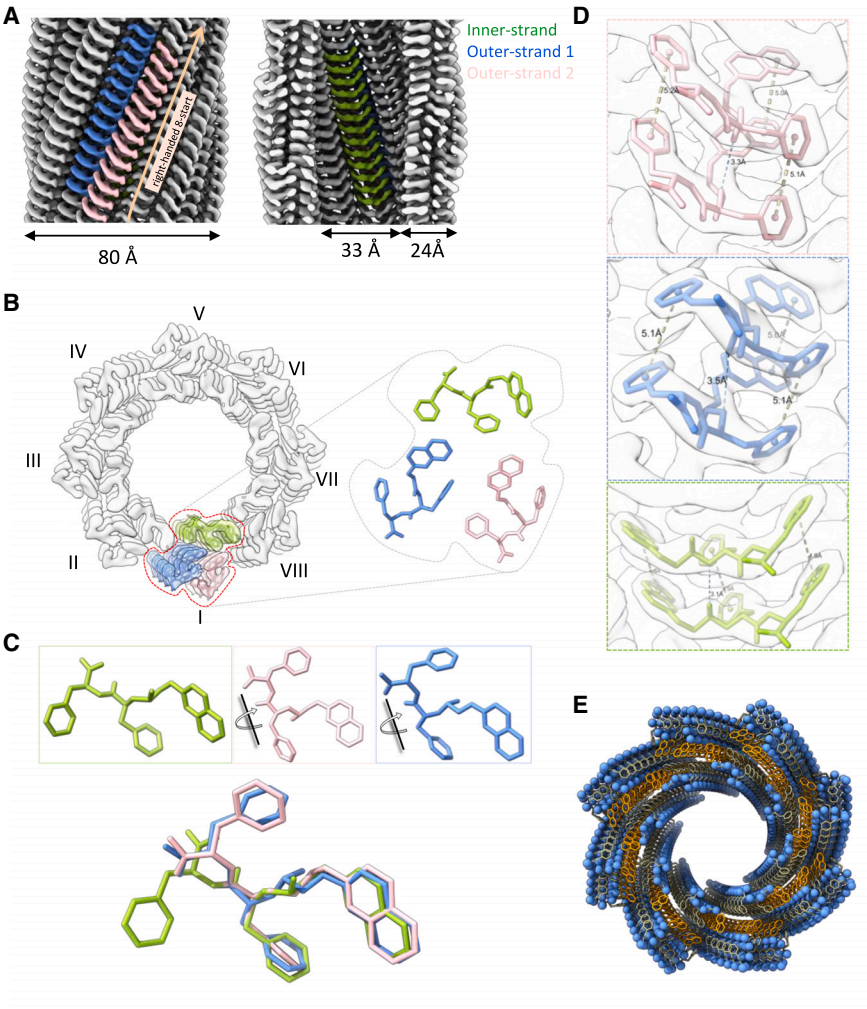

Figure 2. Cryo-EM of LL-tube

(A) Cryo-EM density map of LL-tube.

(B) LL-tube model fit in map from top view. The helical asymmetric unit (ASU) of the LL-tube (right).

(C) Individual structures of the three (L,L)-2NapFF dipeptides and their superimposed view (bottom) present in the ASU of LL-tube.

(D) Interpeptide interaction, π-π stacking, and H-bond in three strands of LL-tube.

(E) Top view of LL-tube atomic structure. The aromatic rings are shown as sticks, and all polar atoms are shown as blue spheres.

group and polar atoms of the peptide backbone on the inner and outer surfaces of the tube (Figure 2E).

We note that the data collected here agree well with the previous low-resolution SANS study, which used contrast-matching approaches to determine the packing within the aggregates.[24]

Cryo-EM structure of (L,D)-2NapFF micelle

Interestingly, the (L,D)-2NapFF oligomerizes into a tube of very different morphology than its stereoisomer, a ~300-Å-wide tube having a thin two-layered wall, which we name the LD-tube (Figure 1C). Its 2D class average (Figure 1C) reveals only a single set of helical striations arising from the top and bottom surfaces of the tube, while

the averaged power spectrum of LD-tube segments (Figure 1D) shows ll extending out to ~3.0 Å. Like the LL-tube, the LD-tube appears to be homogeneous and highly ordered. The reconstruction for the LD-tube was challenging, as there were ~50 possible symmetries that would all be consistent with the power spectrum. These symmetries are defined by an axial rise and a helical rotation relating each ASU, with the possibility that there may also be a rotational point group symmetry. Further complicating the problem, the expected axial rises for closely related symmetries, in some cases differing by only a few thousandths of an Å. For example, ll1 at 1/(21 Å) might contain a Bessel order 28, 29, 30, 31, 32, or 33. Similarly, ll7 at 1/(3 Å) might contain a Bessel order 7, 8, 9, 10, 11, or 12. Now, if we consider two helical symmetries, 31/9 and 32/9, described by the Bessel orders on ll1/ll7, the axial rises for them will be 0.102 and 0.0989 Å, respectively. The difference of 0.003 Å in the axial rise between these two helical symmetries makes their helical nets very similar. In practice, the refinement of the helical symmetry will have many local minima in which the alignment procedure can get stuck.

After exhaustively testing all possible symmetries, we could generate a 3D reconstruction for the LD-tube with a global resolution of 3.3 Å by imposing the symmetry parameters 0.09892 Å/78.6977° (ll1/ll7 orders −32/+9). The hand of the LD-tube was selected using the same procedure employed for the LL-tube. The ratio of the wall thickness of the LD-tube (~20 Å) compared to the tube diameter (~300 Å) is much smaller than in the LL-tube, where the wall thickness and tube diameter were 24 and 80 Å, respectively. The LD-tube is composed of an inner and an outer shell (Figures 3A and 3B) and is a 32-start helical assembly made up of 32 protofilaments, each consisting of two strands forming the inner and outer wall of the tube (Figures 3A and 3B). Unlike the LL-tube, the helical ASU contains two (L,D)-2NapFF dipeptides (one forming the inner wall and the other the outer) having almost identical geometry (Figures 3A and 3B). However, the orientations of naphthalene rings in the inner and outer strands are in opposite directions (Figures 3A and 3B). The basic stacking of dipeptides in each LD-tube strand is similar to that of the LL-tube, i.e., it is mediated by π-π stacking of aromatic rings and a weak H-bond. Like the LL-tube, the LD-tube strands orient all aromatic rings into the space between the inner and outer walls while orienting the carbonyl groups and peptide backbone polar atoms onto the inner and outer surfaces of the tube (Figure 3C).

We prepared partially deuterated analogs of the (L,D)-2NapFF allowing a contrast-matching SANS experiment. Essentially, the deuterated segments of the dipeptide will become invisible to the neutrons.[42,43] As noted above, we previously used this approach to model the packing in the LL-tubes, with the data agreeing with those presented here (Figures 4A and 4B). For the LD-tubes, the data from the SANS experiments can all be fitted to the same model (Figure 4D), showing that there is little change in the dimensions of the structures. However, these data would be hard to rationalize or understand without the cryo-EM structure. Using the cryo-EM structure, we find excellent agreement with the SANS results (Figure 4C). The molecular packing is such that making part of the molecule neutron invisible would not be expected to lead to a change in the overall dimensions of the tube, although a change in intensity of the neutron scattering, as observed, is expected.

Cryo-EM analysis of micelles of (L,L)-2NapFF derivatives

We investigated the morphological characteristics of three distinct micelles formed by derivatives of the 2NapFF dipeptide, namely CarbIF,[44] 3MeOFF,[45] and ThNapFF,[46] which have been recently characterized to form supramolecular gels.

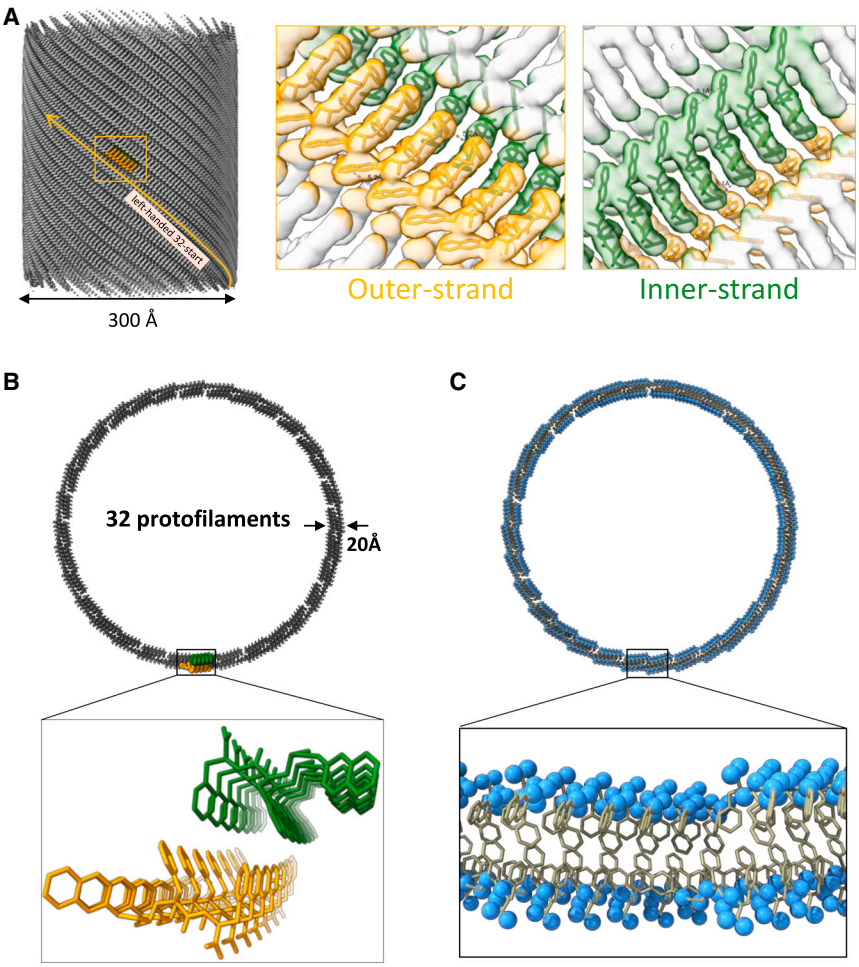

Figure 3. Cryo-EM of LD-tube

(A) Cryo-EM density map of LD-tube. The packing of the (L,D)-2NapFF dipeptide in the outer and inner strands is shown in the middle and on the right.

(B) Top view of LD-tube atomic model showing molecular packing of inner and outer strands.

(C) Top view of LD-tube atomic model. The aromatic rings are shown as sticks, and all polar atoms are shown as blue spheres.

These micelles exhibit varying morphologies despite their closely related chemical compositions.

Our cryo-EM analysis revealed noteworthy differences in the morphological features of these micelles. The CarbIF micelle, as shown in Figure 5A, displayed a tubular structure with a diameter of approximately 88 Å, resembling the LL-tube. However, the packing arrangement of strands in CarbIF appeared to differ, indicated by its smaller diameter (~88 Å) and a discerned helical periodicity of around 110 Å, as observed in the power spectrum (Figure 5B). Conversely, the 3MeOFF micelle exhibited a significantly larger tubular structure akin to the LD-tube, boasting a diameter of approximately 620 Å, nearly twice that of LD-tubes. Interestingly, despite its larger size, the helical periodicity of the 3MeOFF micelle remained consistent with that of the LD-tube, measuring 22 Å (Figures 5C and 5D). In contrast to both LL- and LD-tubes, as well as CarbIF and 3MeOFF micelles, the ThNapFF micelle adopted a worm-like, non-hollow structure, featuring an apparent helical periodicity of approximately 61 Å.

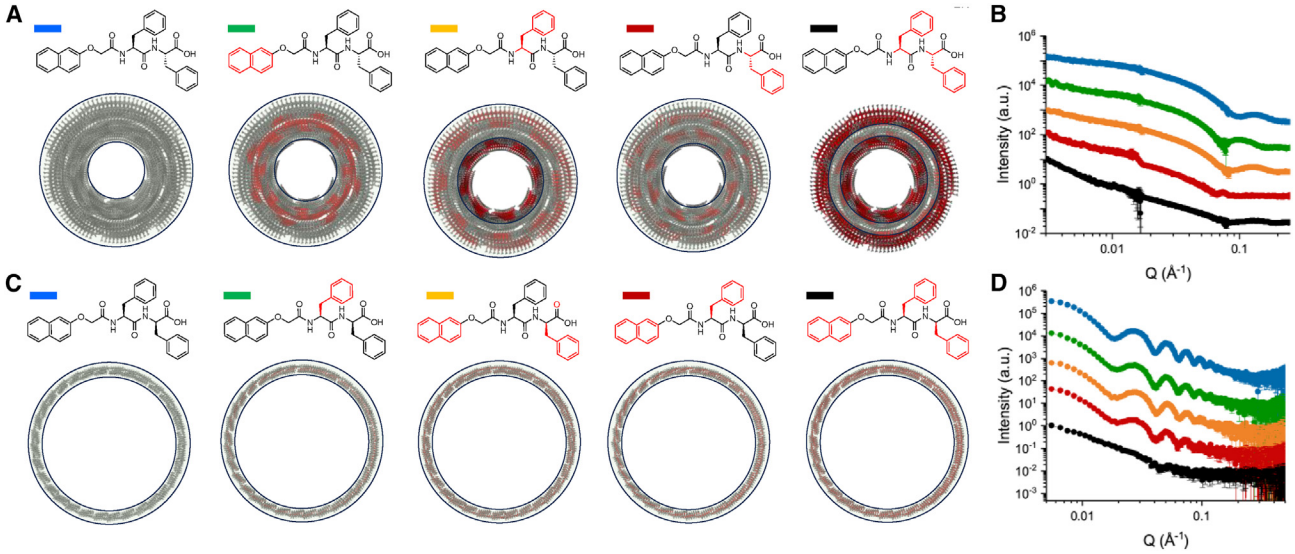

Figure 4. Correlation between SANS data and cryo-EM model of LL-tube and LD-tube

(A and C) Superposition of SANS-derived models of wall thickness and diameter (black circles) for different deuterated constructs (top rows) for (A) LL-tube and (C) LD-tube on the cryo-EM atomic models.

(B and D) SANS curves of deuterated (B) LL-tubes and (D) LD-tubes.

The deuterated region is shown as red (A and C) in both chemical structure (top) and atomic models (bottom). The SANS-derived models for wall thickness correspond to the non-deuterated portions of the molecule, and the models change for the LL-tubes (A) but remain the same for all deuterations of the LD-tubes (C). Refer to Figure S3 and Table S1 for SANS data fitting statistics for LD-tubes.

It is noteworthy that the dimensions of these three micelles, as determined through cryo-EM analysis, corroborate previous observations made using indirect methods.[44–46] Furthermore, our analysis provided the additional information that all three micelles are formed by the highly ordered packing of dipeptides, as evident from the high-resolution features in their respective 2D class averages and the presence of high-resolution II in the corresponding power spectrum (Figure 5).

DISCUSSION

Cryo-EM structures of LL- and LD-tubes not only reveal that they are highly ordered micelles but confirm previous conclusions about packing of these micelles and the gelation phenomenon derived from lower-resolution data. The LL- and LD-tubes are similar in many ways but are remarkably different structures. The fundamental packing of dipeptides in each strand is similar in both tubes, where the dipeptides stack through their aromatic rings and are held together by additional H-bonds. However, the packing of strands into the higher-order assemblies is different for both tubes. Our structures explain why the altered chirality of a single residue produces drastically different micelles. It is clear from the structures that (L,L)-2NapFF can have three different conformations, which give rise to three different types of strands packed in the smaller diameter LL-tube compared to the single type of strand formed by (L,D)-2NapFF that packs together in the larger-diameter LD-tube. Two outer strands align their aromatic rings against those of an inner strand, forming a protofilament, eight of which twist in a right-handed manner to form narrow, hollow LL-tubes. In the LD-tube, the single outer strand aligns against the inner one to make a protofilament, and 32 of them twist in a left-handed manner to form the large, hollow LD-tube. The packing of both the LL- and LD-tubes suggests that the nearest-neighbor interactions in the tubes are driven by burying the aromatic rings in the hydrophobic core while keeping the carbonyl groups solvent accessible.

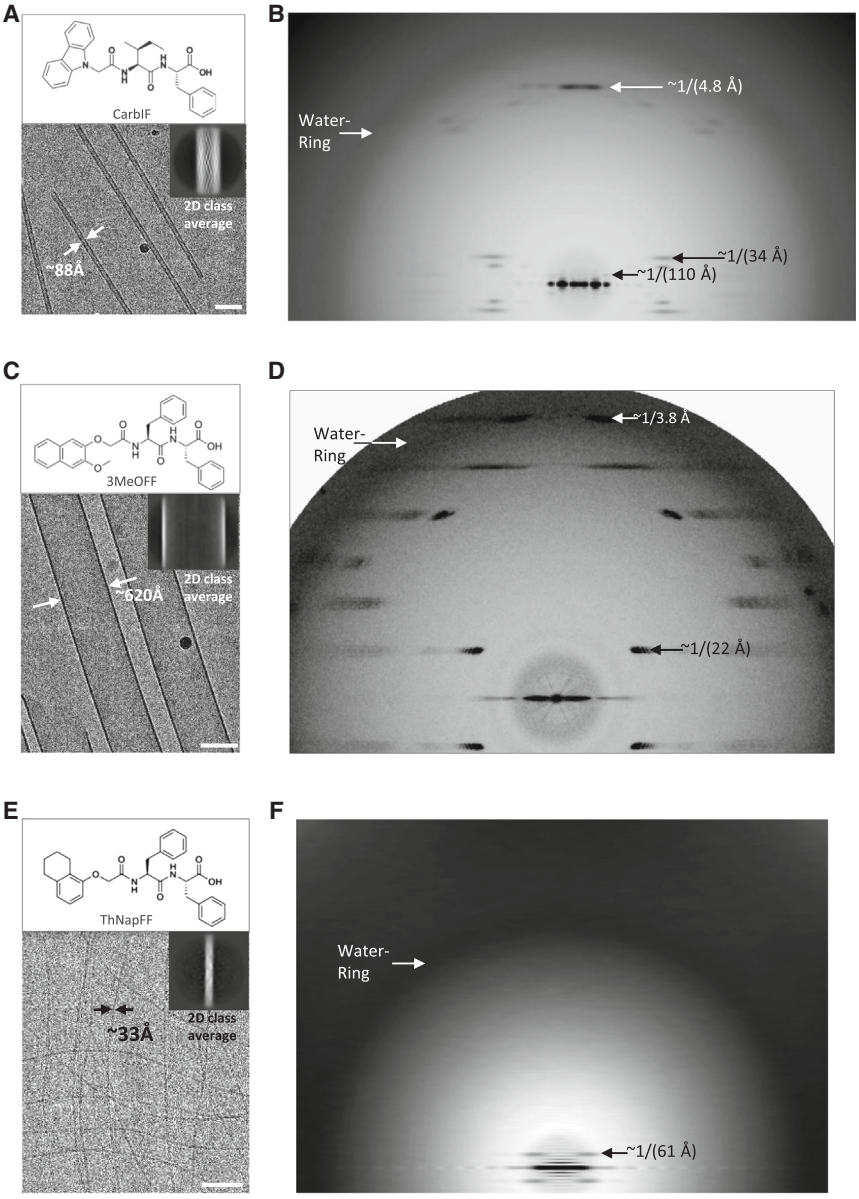

Figure 5. Morphology analysis of micelles from (L,L)-2NapFF derivates by cryo-EM

(A) Chemical structure of CarbIF dipeptide (top) and cryo-EM with 2D class average of its micelle (bottom).

(B) Averaged power spectrum of CarbIF micelle segments. Layer lines with their associated Bessel orders are labeled. The diffuse water ring, at ~ 1/(3.7 Å), arises from the average separation of water molecules being ~3.7 Å.

(C) Chemical structure of 3MeOFF dipeptide (top) and cryo-EM with 2D class average of its micelle (bottom).

(D) Averaged power spectrum of 3MeOFF micelle segments, with two layer lines and the water ring labeled.

(E) Chemical structure of ThNapFF dipeptide (top) and cryo-EM with 2D class average of its micelle (botom).

(F) Averaged power spectrum of ThNapFF micelle segments, with a layer line and the water ring labeled. Scale bar: ~50 nm.

The overall dimensions of tubes and the orientation of aromatic rings and carbonyl groups seen in the cryo-EM structures match well with prior models from SAXS, SANS, and atomistic molecular dynamics stimulation data.[24,38] The morphology of both tubes is very straight, arising from a structural rigidity. They do not appear to aggregate at high pH in micellar forms, as no side-by-side stacking of tubes is apparent in cryo-EM images. In contrast, at low pH, it was previously observed that they start to stick and entangle with each other, as evident from the gelation.[47] It is of note that the outer and inner surfaces of both tubes contain the exposed carbonyl groups. At high pH, the carbonyl tends to be deprotonated, and the overall charge on both surfaces will be highly negative. It has been demonstrated in polymer-electrolyte physics that a polymer with uniformly charged functional groups on its surface adopts a straight conformation because of same-sign charge repulsion.[48,49] Such charge repulsion between carbonyl groups of LL- and LD-tubes would resist tube bending and favor the straight morphology. Same-sign charge repulsion could also prevent the aggregation of tubes in micellar form at high pH.

Cryo-EM structures of LL- and LD-tubes shed further light on their gelation mechanism. Both LL- and LD-tubes form gels upon lowering the pH.[38] The previous SAXS and SANS data suggest that the LL-tube transforms from a hollow cylinder to a (non-hollow) elliptical rod structure at low pH. As the pH is decreased, protonation of the carbonyl groups present on both the inner and outer surfaces of the tube masks the apparent negative charge on tube surfaces and allows for tube bending and inter-tube interactions leading to gel formation. In the absence of charge-charge repulsion, the inner walls collapse at low pH to form an elliptical rod; indeed, previous data show that this aggregate has two apparent pK_a values, with the highest (around 9) being ascribed to the carboxylic acid in the inner wall.[24] The close proximity of these groups as shown in the cryo-EM structure explains this high value for a carboxylic acid on the basis of the packing leading to strong ion-dipole interactions between $RCOO^-$ and RCOOH, stabilizing the charge. In contrast, the inner walls of LD-tubes do not collapse upon pH reduction and maintain a large tubular structure with slight change in overall dimensions.[38] Our hypothesis is that the lower curvature in the walls means that losing local order in the walls does not lead to collapse overall, as charge balance is maintained as the pH is decreased. Hence, protonation results in a removal of charge, allowing the tubes to come together to form a gel, but no inner wall collapse.

There are many chemical derivatives of 2NapFF that form micelles of different dimensions.[44–46] The knowledge that the fundamental assembly of 2NapFF is driven by systematic π-π stacking and that the long-range stiffness is likely mediated by the negatively charged carbonyl groups will be crucial in rational design strategies for the modification of these compounds. The cryo-EM approach used here improves our knowledge of these systems immensely, moving away from cartoon-like structures, and allows us to understand aspects such as the multiple pK_a values, as well as why specific structures change upon pH adjustment while others change far less. The data here explain the contrast-matching SANS experiments. While the SANS and cryo-EM experiments are complementary, the SANS experiments require significant, expensive synthesis as well the assumption that deuteration does not lead to structural changes. The near-atomic resolution that has now become routine with the cryo-EM approach should lead to the determination of many non-biological supramolecular structures and directly address whether specific functional groups are accessible for specific reactions or as catalytic sites.[50,51]

EXPERIMENTAL PROCEDURES

Resource availability

Lead contact

Further information and requests for resources and reagents should be directed to the lead contact, Edward H. Egelman (egelman@virginia.edu).

Materials availability

This study did not generate new unique reagents.

Data and code availability

Atomic models of LL- and LD-tubes are provided as Data S1 and S2, respectively. Cryo-EM maps of LL- and LD-tubes have been deposited in the Electron Microscopy Data Bank with accession IDs EMD-42434 and EMD-42436, respectively.

Materials preparation

(L,L)-2NapFF and (L,D)-2NapFF were synthesized as described elsewhere.[38] The partially deuterated analogs of (L,D)-2NapFF were prepared using similar procedures. Full synthetic and characterization details are described in the supplemental information (supplemental experimental procedures; Figures S4–S40).

Preparation of LL and LD tubes

500 mg either (L,L)-2NapFF or (L,D)-2NapFF was suspended in deionized water. To this suspension was added one molar equivalent of a sodium hydroxide solution (0.1 M, NaOH, Sigma-Aldrich) such that the final volume was 50 mL. The solution was stirred at 1,200 rpm overnight to allow complete dissolution of the gelator. At this point, all solid had dissolved, and a free-flowing, viscous solution was formed. Finally, the pH of each solution was measured and adjusted if necessary to pH 11 $\pm$ 0.1 using either NaOH (1 M) or HCl (1 M) as appropriate.

Vitrification of sample on copper grid for cryo-EM

3 μL tube suspensions were applied on glow discharged lacey carbon grids, and excessive sample was blotted away, leaving a thin film of sample on the grid, which was plunge frozen in liquid ethane using a Vitrobot Mark IV (Thermo Fisher Scientific). Frozen grids were stored in liquid nitrogen until the cryo-EM experiment.

Cryo-EM

Cryo-EM data collection and image preprocessing

The frozen grids were screened on a 200 keV electron microscope (Glacios, Thermo Fisher Scientific) for selection of grids with the best ice thickness and tube distribution. The best grid was used for full data collection on a 300 keV electron microscope (Titan Krios, Thermo Fisher Scientific) equipped with a K3 direct electron detector (Gatan). Dose-fractioned movies were recorded by total exposure per movie of ~50 e $Å^{-2}$ with pixel sizes of ~0.67 and ~1.08 Å for LL- and LD-tubes, respectively. Beam-induced and full-frame motions in raw movies were corrected by the "patch motion correction" job in cryoSPARC.[52] Motion-corrected movies were used for the CTF estimation by the "patch CTF estimation" job in cryoSPARC.[52]

Reconstructions of LL- and LD-tube volume map

The 3D reconstructions of LL- and LD-tubes were performed using the helical processing workflow in cryoSPARC.[52] Tube segments were manually boxed from only a few micrographs to generate 2D class averages for further automatic template-based particle picking by "filament tracer." The averaged power spectra of vertically aligned segments of tubes were generated for both tubes and used for indexing,

which yields the helical parameters. Almost ~5 and more than ~50 symmetries were calculated for LL- and LD-tubes, respectively, from the power spectra. Initial volumes for LD-tubes were generated using SPIDER and were then used as starting models for reconstructions in cryoSPARC. The "helix refine" job in cryoSPARC was used for the reconstruction of both tubes. The maps were further improved by iterative cycles of refinements with different options like "non-uniform refinement," "local-CTF refinement," and map sharpening by deepEMhancer.[53]

Cryo-EM data collection and processing statistics are provided in the supplemental information (Table S2). The local resolution maps and map-to-map FSC curves generated from cryoSPARC for both LL- and LD-tubes are provided in the supplemental information (Figures S1 and S2).

Model building

The PDB models for (L,L)-2NapFF and (L,D)-2NapFF with geometry restrain were generated using *Phenix.elbow*.[54] The PDB models were rigid-body fit into the respective maps. The models were further refined by iterative cycles of interactive refinement in COOT[55] and automatic refinement by Phenix Real Space Refinement.[54] The model fitting statistics are provided in the supplemental information (Table S2).

Structural analysis

Structural analysis and representation were performed using ChimeraX.[56]

Sample preparation for SANS measurements

Solutions of different hydrogenated and partially deuterated (L,D)-2NapFF at 10 mg/mL were prepared as follows: 50 mg (L,D)-2NapFF was weighed into a 7 mL Sterilin vial. Then, 4 mL D_2O was added, followed by 1 mL of a solution of NaOD in D_2O (0.1 M, diluted in D_2O using the commercially available 40 wt % solution, Sigma-Aldrich). The solutions were stirred overnight at 1,000 rpm until dissolution. Once dissolved, the pH was adjusted to 11 using 1 M NaOH.

SANS measurement and analysis

SANS experiments were performed using the ZOOM instrument at the ISIS Neutron and Muon source of the STFC Rutherford Appleton Laboratory (Didcot, UK), experiment numbers RB2310030 and RB2310049. The samples were measured using a sample changer and a water bath at 25°C. The source-to-sample/sample-to-detector distance was set to L1 = L2 = 8 m to access a q range of 0.0045–0.8 $Å^{-1}$, where $q = 4\pi\sin(\theta/2)/\lambda$ using neutrons of wavelengths spanning 1.57–14.6 Å. All solutions were measured in UV-spectrophotometer-grade quartz cuvettes (Hellma) with 2 mm path length. The 2D scattering patterns were azimuthally integrated to obtain 1D plots of intensity vs. Q using the facility-provided software. The scattering from the D_2O background and the empty cell were subtracted from the gelator solutions using MantidPlot, and SANS curves were fitted using SasView (v.4.2.0, http://www.sasview.org/). The SANS plots and fitting parameters are provided in the supplemental information (Figure S3; Table S1).

SUPPLEMENTAL INFORMATION

Supplemental information can be found online at https://doi.org/10.1016/j.xcrp.2024.101812.

ACKNOWLEDGMENTS

D.J.A. thanks the EPSRC for a fellowship (EP/L021978/2), which also funded B.D. E.R.D. thanks the UKRI (MR/V021087/1) for funding a Future Leaders Fellowship. We acknowledge the University of Virginia Molecular Electron Microscopy Core facility, where the electron microscopy was performed. We acknowledge STFC beamtime allocation RB2310030 and RB2310049 on ZOOM, DOI: 10.5286/ISIS.E.RB 2310030, at the ISIS Neutron and Muon Source, Didcot, UK. This work benefited from SasView software, originally developed by the DANSE project under NSF award DMR-0520547. E.H.E. was funded by NIH grant GM122510. Names of chemical structures were generated using Marvin Sketch 22.16 (www.chemaxon.com). We thank Tomek Osinski for computational support.

AUTHOR CONTRIBUTIONS

D.J.A. and E.H.E. conceptualized the project. R.R.S. and E.H.E. performed the cryo-EM experiment and data processing. S.B., B.D., J.D., E.R.D., and D.J.A. prepared the samples and performed the SANS experiment. R.R.S., D.J.A., and E.H.E. wrote the paper.

DECLARATION OF INTERESTS

The authors declare no competing interests.

Received: November 17, 2023
Revised: January 9, 2024
Accepted: January 12, 2024
Published: January 31, 2024

REFERENCES

1. Du, X., Zhou, J., Shi, J., and Xu, B. (2015). Supramolecular hydrogelators and hydrogels: from soft matter to molecular biomaterials. Chem. Rev. *115*, 13165–13307.
2. Fleming, S., and Ulijn, R.V. (2014). Design of nanostructures based on aromatic peptide amphiphiles. Chem. Soc. Rev. *43*, 8150–8177.
3. Fichman, G., and Gazit, E. (2014). Self-assembly of short peptides to form hydrogels: Design of building blocks, physical properties and technological applications. Acta Biomater. *10*, 1671–1682.
4. Lampel, A. (2020). Biology-inspired supramolecular peptide systems. Chem *6*, 1222–1236.
5. Conticello, V.P. (2023). Peptide-based nanomaterials: Building back better & beyond. Curr. Opin. Solid State Mater. Sci. *27*, 101066.
6. Bera, S., Basu, S., Jana, B., and Dastidar, P. (2023). Real-time Observation of Macroscopic Helical Morphologies under Optical Microscope: A Curious Case of π–π Stacking Driven Molecular Self-assembly of an Organic Gelator Devoid of Hydrogen Bonding. Angew. Chem. Int. Ed. Engl. *62*, e202216447.
7. Corbet, C.H.W.A., van den Bersselaar, B.W.L., de Waal, B.F.M., Reynaerts, R., Mali, K.S., De Feyter, S., Jonas, A.M., Meijer, E.W., and Vantomme, G. (2023). Self-assembly of Discrete Oligomers of Naphthalenediimides in Bulk and on Surfaces. Chemistry (Basel). e202303107.
8. Ross, C.A., and Poirier, M.A. (2004). Protein aggregation and neurodegenerative disease. Nat. Med. *10*, S10–S17.
9. Haass, C., and Selkoe, D.J. (2007). Soluble protein oligomers in neurodegeneration: lessons from the Alzheimer's amyloid β-peptide. Nat. Rev. Mol. Cell Biol. *8*, 101–112.
10. Levin, A., Hakala, T.A., Schnaider, L., Bernardes, G.J.L., Gazit, E., and Knowles, T.P.J. (2020). Biomimetic peptide self-assembly for functional materials. Nat. Rev. Chem *4*, 615–634.
11. Sitsanidis, E.D., Dutra, L.A.L., Schirmer, J., Chevigny, R., Lahtinen, M., Johansson, A., Piras, C.C., Smith, D.K., Tiirola, M., Pettersson, M., and Nissinen, M. (2023). Probing the Gelation Synergies and Anti-Escherichia coli Activity of Fmoc-Phenylalanine/Graphene Oxide Hybrid Hydrogel. ACS Omega *8*, 10225–10234.
12. Boekhoven, J., Hendriksen, W.E., Koper, G.J.M., Eelkema, R., and van Esch, J.H. (2015). Transient assembly of active materials fueled by a chemical reaction. Science *349*, 1075–1079.
13. Mandal, D., Nasrolahi Shirazi, A., and Parang, K. (2014). Self-assembly of peptides to nanostructures. Org. Biomol. Chem. *12*, 3544–3561.
14. Sang, Y., and Liu, M. (2019). Nanoarchitectonics through supramolecular gelation: formation and switching of diverse nanostructures. Mol. Syst. Des. Eng. *4*, 11–28.
15. Ghosh, G. (2023). Pathway dependent controlled supramolecular polymerization of peptides. Giant *14*, 100160.
16. Yu, G., Yan, X., Han, C., and Huang, F. (2013). Characterization of supramolecular gels. Chem. Soc. Rev. *42*, 6697–6722.
17. Dastidar, P., Roy, R., Parveen, R., and Sarkar, K. (2019). Supramolecular synthon approach in designing molecular gels for advanced therapeutics. Advanced Therapeutics *2*, 1800061.
18. Meazza, L., Foster, J.A., Fucke, K., Metrangolo, P., Resnati, G., and Steed, J.W. (2013). Halogen-bonding-triggered supramolecular gel formation. Nat. Chem. *5*, 42–47.
19. Farahani, A.D., Martin, A.D., Iranmanesh, H., Bhadbhade, M.M., Beves, J.E., and Thordarson, P. (2019). Gel-and Solid-State-Structure of Dialanine and Diphenylalanine Amphiphiles: Importance of C…H Interactions in Gelation. ChemPhysChem *20*, 972–983.
20. Ghosh, D., Farahani, A.D., Martin, A.D., Thordarson, P., and Damodaran, K.K. (2020). unraveling the self-assembly modes in multicomponent supramolecular gels using single-crystal X-ray diffraction. Chem. Mater. *32*, 3517–3527.

21. Giuri, D., Marshall, L.J., Wilson, C., Seddon, A., and Adams, D.J. (2021). Understanding gel-to-crystal transitions in supramolecular gels. Soft Matter *17*, 7221–7226.

22. Mears, L.L.E., Draper, E.R., Castilla, A.M., Su, H., Zhuola, Dietrich, B., Dietrich, B., Nolan, M.C., Smith, G.N., Doutch, J., Rogers, S., et al. (2017). Drying affects the fiber network in low molecular weight hydrogels. Biomacromolecules *18*, 3531–3540.

23. Bernal, J.D., Fankuchen, I., and Perutz, M. (1938). An X-ray study of chymotrypsin and haemoglobin. Nature *141*, 523–524.

24. Draper, E.R., Dietrich, B., McAulay, K., Brasnett, C., Abdizadeh, H., Patmanidis, I., Marrink, S.J., Su, H., Cui, H., Schweins, R., et al. (2020). Using small-angle scattering and contrast matching to understand molecular packing in low molecular weight gels. Matter *2*, 764–778.

25. Egelman, E.H. (2016). The Current Revolution in Cryo-EM. Biophys. J. *110*, 1008–1012.

26. Bai, X.C., McMullan, G., and Scheres, S.H.W. (2015). How cryo-EM is revolutionizing structural biology. Trends Biochem. Sci. *40*, 49–57.

27. Kühlbrandt, W. (2014). Cryo-EM enters a new era. Elife *3*, e03678.

28. Wang, F., Gnewou, O., Solemanifar, A., Conticello, V.P., and Egelman, E.H. (2022). Cryo-EM of Helical Polymers. Chem. Rev. *122*, 14055–14065.

29. Deshmukh, A., Zheng, W., Chuang, C., Bailey, A., Williams, J., Sletten, E., Egelman, E., and Caram, J. (2023). Near-Atomic Resolution Structure of J-Aggregated Helical Light Harvesting Nanotubes. Preprint at ChemRxiv. https://doi.org/10.26434/chemrxiv-2022-5m8sx.

30. Yang, Z., Liang, G., Ma, M., Gao, Y., and Xu, B. (2007). Conjugates of naphthalene and dipeptides produce molecular hydrogelators with high efficiency of hydrogelation and superhelical nanofibers. J. Mater. Chem. *17*, 850–854.

31. Hamley, I.W. (2023). Self-assembly, bioactivity, and nanomaterials applications of peptide conjugates with bulky aromatic terminal groups. ACS Appl. Bio Mater. *6*, 384–409.

32. Mahler, A., Reches, M., Rechter, M., Cohen, S., and Gazit, E. (2006). Rigid, self-assembled hydrogel composed of a modified aromatic dipeptide. Adv. Mater. *18*, 1365–1370.

33. Smith, A., Williams, R., Tang, C., Coppo, P., Collins, R., Turner, M., Saiani, A., and Ulijn, R. (2008). Fmoc-diphenylalanine self assembles to a hydrogel via a novel architecture based on π–π interlocked β-sheets. Adv. Mater. *20*, 37–41.

34. Tang, C., Smith, A.M., Collins, R.F., Ulijn, R.V., and Saiani, A. (2009). Fmoc-diphenylalanine self-assembly mechanism induces apparent p K a shifts. Langmuir *25*, 9447–9453.

35. Martin, A.D., Wojciechowski, J.P., Robinson, A.B., Heu, C., Garvey, C.J., Ratcliffe, J., Waddington, L.J., Gardiner, J., and Thordarson, P. (2017). Controlling self-assembly of diphenylalanine peptides at high pH using heterocyclic capping groups. Sci. Rep. *7*, 43947.

36. Yang, Z., Gu, H., Du, J., Gao, J., Zhang, B., Zhang, X., and Xu, B. (2007). Self-assembled hybrid nanofibers confer a magnetorheological supramolecular hydrogel. Tetrahedron *63*, 7349–7357.

37. Cardoso, A.Z., Mears, L.L.E., Cattoz, B.N., Griffiths, P.C., Schweins, R., and Adams, D.J. (2016). Linking micellar structures to hydrogelation for salt-triggered dipeptide gelators. Soft Matter *12*, 3612–3621.

38. McAulay, K., Dietrich, B., Su, H., Scott, M.T., Rogers, S., Al-Hilaly, Y.K., Cui, H., Serpell, L.C., Seddon, A.M., Draper, E.R., and Adams, D.J. (2019). Using chirality to influence supramolecular gelation. Chem. Sci. *10*, 7801–7806.

39. Henderson, R., Sali, A., Baker, M.L., Carragher, B., Devkota, B., Downing, K.H., Egelman, E.H., Feng, Z., Frank, J., Grigorieff, N., et al. (2012). Outcome of the first electron microscopy validation task force meeting. Structure *20*, 205–214.

40. Subramaniam, S., Earl, L.A., Falconieri, V., Milne, J.L., and Egelman, E.H. (2016). Resolution advances in cryo-EM enable application to drug discovery. Curr. Opin. Struct. Biol. *41*, 194–202.

41. Pieri, L., Wang, F., Arteni, A.A., Vos, M., Winter, J.M., Le Du, M.H., Artzner, F., Gobeaux, F., Legrand, P., Boulard, Y., et al. (2022). Atomic structure of Lanreotide nanotubes revealed by cryo-EM. Proc. Natl. Acad. Sci. USA *119*, e2120346119.

42. Melnichenko, Y.B., and Wignall, G.D. (2007). Small-angle neutron scattering in materials science: Recent practical applications. J. Appl. Phys. *102*.

43. Bendedouch, D., Chen, S.H., and Koehler, W.C. (1983). Structure of ionic micelles from small angle neutron scattering. J. Phys. Chem. *87*, 153–159.

44. Marshall, L.J., Bianco, S., Ginesi, R.E., Doutch, J., Draper, E.R., and Adams, D.J. (2023). Investigating multigelator systems across multiple length scales. Soft Matter *19*, 4972–4981.

45. McAulay, K., Wang, H., Fuentes-Caparrós, A.M., Thomson, L., Khunti, N., Cowieson, N., Cui, H., Seddon, A., and Adams, D.J. (2020). Isotopic control over self-assembly in supramolecular gels. Langmuir *36*, 8626–8631.

46. Huang, R., McDowall, D., Ng, H., Thomson, L., Al-Hilaly, Y.K., Doutch, J., Burholt, S., Serpell, L.C., Poole, R.J., and Adams, D.J. (2022). Charge screening wormlike micelles affects extensional relaxation time and noodle formation. Chem. Commun. *58*, 10388–10391.

47. Draper, E.R., Su, H., Brasnett, C., Poole, R.J., Rogers, S., Cui, H., Seddon, A., and Adams, D.J. (2017). Opening a can of worm (-like micelle) s: the effect of temperature of solutions of functionalized dipeptides. Angew. Chem. Int. Ed. Engl. *56*, 10467–10470.

48. Skolnick, J., and Fixman, M. (1977). Electrostatic Persistence Length of a Wormlike Polyelectrolyte. Macromolecules *10*, 944–948.

49. Odijk, T. (1977). Polyelectrolytes near the rod limit. J. Polym. Sci. Polym. Phys. Ed. *15*, 477–483.

50. Liu, Q., Kuzuya, A., and Wang, Z.-G. (2023). Supramolecular enzyme-mimicking catalysts self-assembled from peptides. iScience *26*, 105831.

51. Liu, N., Li, S.-B., Zheng, Y.-Z., Xu, S.-Y., and Shen, J.-S. (2023). Minimalistic Artificial Catalysts with Esterase-Like Activity from Multivalent Nanofibers Formed by the Self-Assembly of Dipeptides. ACS Omega *8*, 2491–2500.

52. Punjani, A., Rubinstein, J.L., Fleet, D.J., and Brubaker, M.A. (2017). cryoSPARC: algorithms for rapid unsupervised cryo-EM structure determination. Nat. Methods *14*, 290–296.

53. Sanchez-Garcia, R., Gomez-Blanco, J., Cuervo, A., Carazo, J.M., Sorzano, C.O.S., and Vargas, J. (2021). DeepEMhancer: a deep learning solution for cryo-EM volume post-processing. Commun. Biol. *4*, 874.

54. Afonine, P.V., Poon, B.K., Read, R.J., Sobolev, O.V., Terwilliger, T.C., Urzhumtsev, A., and Adams, P.D. (2018). Real-space refinement in PHENIX for cryo-EM and crystallography. Acta Cryst D *74*, 531–544.

55. Emsley, P., and Cowtan, K. (2004). Coot: model-building tools for molecular graphics. Acta Crystallogr. D Biol. Crystallogr. *60*, 2126–2132.

56. Goddard, T.D., Huang, C.C., Meng, E.C., Pettersen, E.F., Couch, G.S., Morris, J.H., and Ferrin, T.E. (2018). UCSF ChimeraX: Meeting modern challenges in visualization and analysis. Protein Sci. *27*, 14–25.